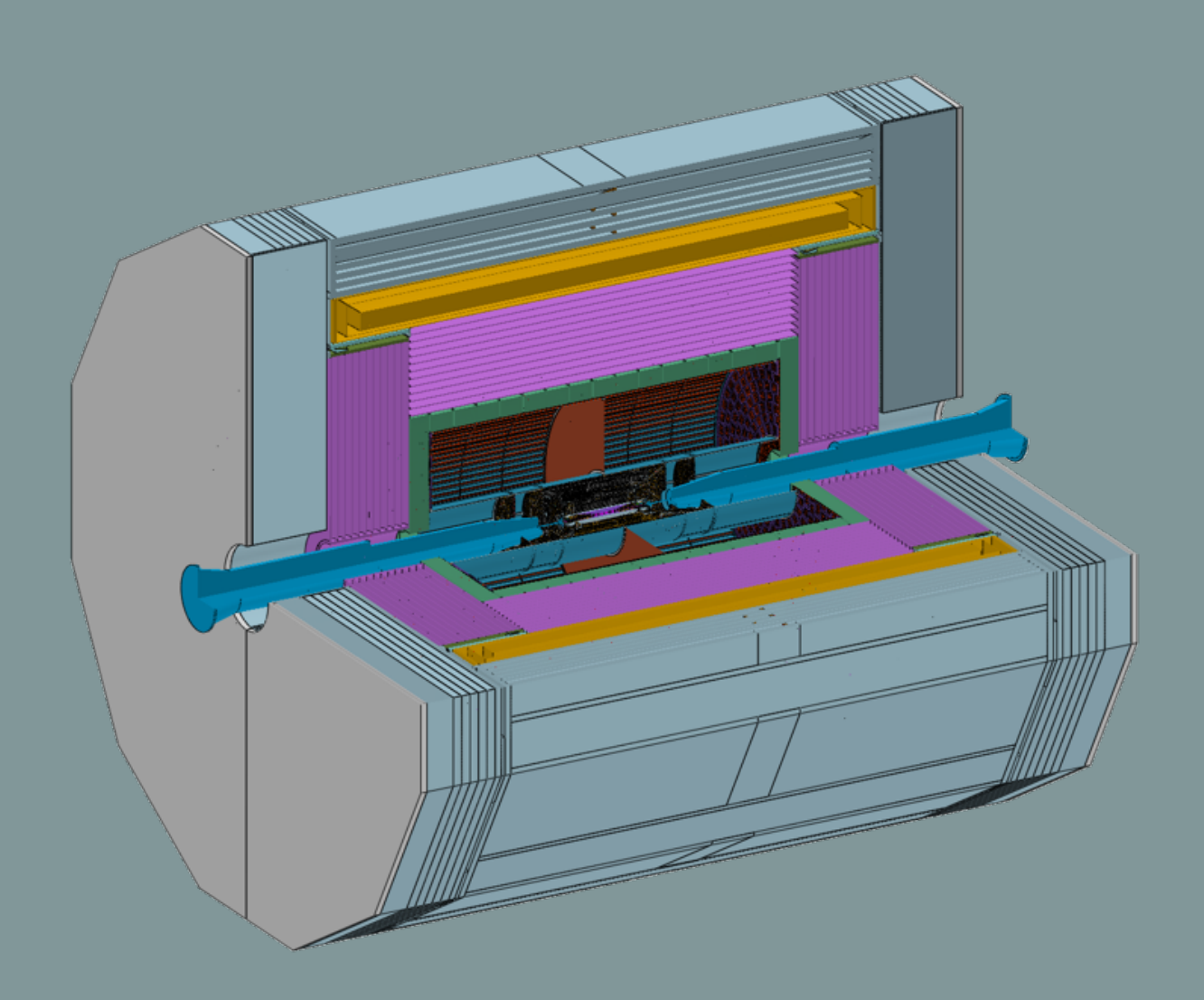
Draft vo. 7HEP-CEPC-DR-2025-01 HEP-EP-2025-01

CEPC Reference Detector Technical Design Report

Version: v0.7.1 build: 2025-11-04 00:48:10Z



The CEPC Study Group October, 2025

Draft v0.7.1

Contents

11	I CE	CPC R	eference Detector	1
12	Chapte	r 3 Ma	achine Detector Interface and luminosity measurement	3
13	3.1	Intera	ction Region	. 3
14	3.2	.2 Detector beam pipe and final focusing system		. 4
15		3.2.1	Detector beam pipe	. 4
16		3.2.2	Final focusing magnets	. 9
17	3.3	Beam	Beam-induced backgrounds	
18		3.3.1	Sources of beam-induced backgrounds	. 10
19		3.3.2	Simulation methods	. 13
20		3.3.3	Beam-induced background studies with BEPCII/BESIII	. 14
21		3.3.4	Mitigation methods	. 15
22		3.3.5	Beam-induced background results	. 18
23	3.4	Luminosity measurement		. 20
24		3.4.1	Introduction	. 20
25		3.4.2	Fast luminosity monitor	. 23
26		3.4.3	Beam position monitor	. 27
27		3.4.4	LumiCal	. 27
28	3.5	Summary and future plans		. 36
29	References			. 36
30	II O	ther C	EPC Detector Concepts	39
31 Glossary				41

Chapter 3 Machine Detector Interface and luminosity measurement

adopted. This factor has already been incorporated into the background calculations presented in Table 3.6. Detailed distributions of hits across the detector are calculated. More in-depth discussions on the impact of BIBs on detectors are presented in the respective sub-detector chapters.

The distributions of TID and NIEL, caused by the considered BIB sources in Higgs mode are shown in Figure 3.12. These were obtained by simulating the absorbed dose and the 1-MeVsilicon equivalent fluence using FLUKA. The operational time is assumed to be 7000 hours per year. The highest TID in the whole detector region is lower than 0.2 MGy per year, while the highest level of NIEL is in the order of 10^{13} (1 MeV n_{eq})/cm² per year. These average dose value and the distribution of TID and NIEL based on a simplified FLUKA model have also been given to sub-detector designers for reference.

With the current IR design, background levels are acceptable for most sub-detectors. However, in high luminosity Z mode, which has a luminosity almost two orders of magnitude higher than the Higgs mode, further optimization must be conducted. It is aimed to achieve a lightweight and efficient design through more optimized mitigation methods. It should be noted that the results and work presented have considered only the ideal beam conditions. In the future, more realistic scenarios must be carefully studied. These include non-ideal beam conditions (e.g., changes in beam orbit, tuning and commissioning phases, and magnet misalignment), as well as currently unaddressed items including injection backgrounds and failure cases like sudden beam loss.

3.4 Luminosity measurement

3.4.1 Introduction

The high event statistics foreseen at the CEPC require that the luminosity be measured with a precision better than 10^{-4} at the *Z*-pole for precision measurements of multiple Standard Model (SM) processes. The e^+e^- collision luminosity is determined by measuring the rate of the Bhabha elastic scattering. The Quantum ElectroDynamics (QED) prediction for Bhabha scattering is with high precision, including complete Next-To-Leading Order (NLO) corrections, which encompass processes such as $e^+e^- \rightarrow e^+e^-\gamma$. The BHLUMI event generator, which was developed at the LEP for calculating low-angle Bhabha cross sections, has achieved a precision of 0.037% [26, 27]. Ongoing efforts aim to improve higher-order corrections, driven by the precision requirement of 10^{-4} at future e^+e^- colliders. The leading-order Bhabha cross section, integrated over the angular coverage ($\theta_{min} < \theta < \theta_{max}$), is given by

$$\sigma = \frac{16\pi\alpha^2}{s} \left(\frac{1}{\theta_{min}^2} - \frac{1}{\theta_{max}^2} \right) \tag{3.1}$$

The integrated luminosity (\mathcal{L}) can be determined from the number of detected Bhabha events

Draft VO 3.4 Luminosity measurement

 N_{acc} , using the following equation:

$$\mathcal{L} = \frac{1}{\epsilon} \frac{N_{acc}}{\sigma}, \quad \frac{\Delta \mathcal{L}}{\mathcal{L}} \approx \frac{2\Delta \theta}{\theta_{min}}$$
 (3.2)

where ϵ is the detection efficiency to be evaluated. The primary sources of systematic uncertainties are errors in θ_{min} , which arise from mechanical alignment and detector resolution. These errors propagate to the luminosity measurement with a factor of two. To achieve the targeted 10^{-4} uncertainty in luminosity, assuming a θ_{min} threshold of 20 mrad for Bhabha events, the corresponding angular deviation $|\Delta\theta|$ is 1 µrad. At a distance of |z| = 1 m from the IP, this translates to a tolerance of 1 µm.

Bhabha events are identified by pairs of electrons and positrons that are back-to-back, each carrying a momentum equal to the beam energy. At the CEPC, these events are measured using the LumiCal, the BPM located near the interaction region (IP BPM), and the FastLumi. These systems are symmetrically installed on both sides of the IP ($\pm z$ directions) and upstream of the cryomodule. A schematic layout on one side shown in Figure 3.13 illustrates their arrangement. The LumiCal, composed of two silicon detectors and two LYSO crystal parts, is installed inside the detector beam pipe. It covers the low-angle region, defined by polar angles $|\theta| < 100$ mrad in the laboratory frame. The FastLumi is a diamond-based detector positioned to cover the very forward region around $|\theta| \sim 10$ mrad. Two BPMs are deployed on each side, with one located inside the flange and the other on the dual beam pipes. In the following, the design of the three detectors is discussed.

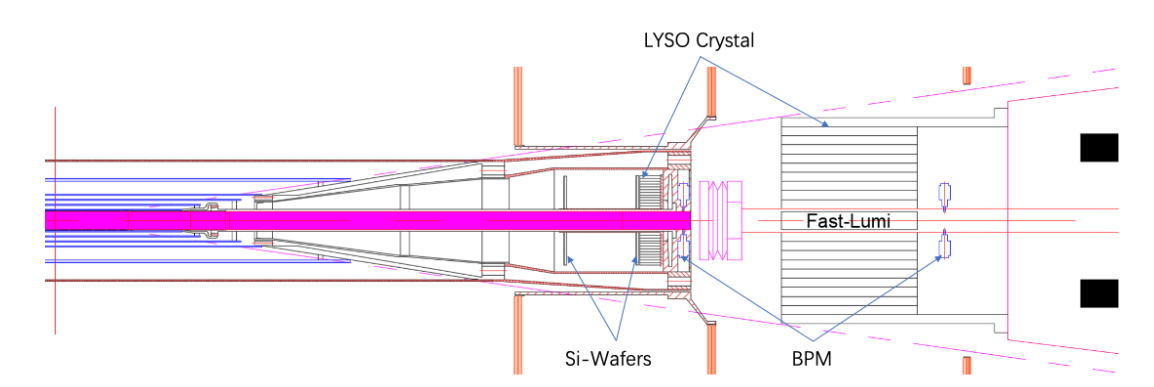


Figure 3.13: The luminosity measurement detectors are shown. Those detectors include the LumiCal, the FastLumi and the BPM. The LumiCal consists of two silicon detectors and two LYSO crystal parts. Before the flange, the Si-wafers combined with short LYSO crystals, provide the electron θ position with the e/γ veto functionality. The long LYSO located behind the bellow is designed to identify beam electrons through energy deposits.

The location of LumiCal is favorable for a lower θ_{min} to increase the Bhabha cross section due to its $1/\theta^2$ dependence. The front LumiCal silicon sensor is located at |z| = 560 mm. The race-track beam pipe has an inner radius of 10 mm. Assuming the detector acceptance edge is 12 mm from the beam pipe center, the corresponding θ_{min} is 21.4 mrad. The outer radii of the first and second Si-wafers are 42 mm and 51 mm, respectively. The outer radii of the short

Chapter 3 Machine Detector Interface and luminosity measurement

and long LYSO modules are 56 mm and 110 mm, respectively. Figure 3.13 illustrates LumiCal, including the silicon wafers, and the LYSO crystals.

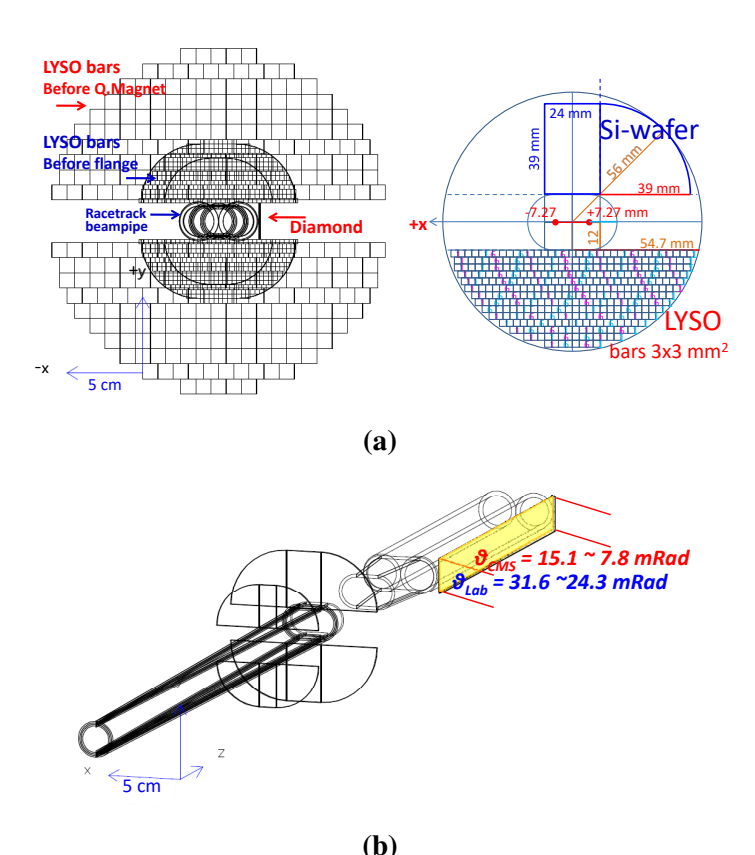


Figure 3.14: The projection of the LumiCal design is illustrated in (a), with the racetrack beam pipe extending from the IP to the quadrupole. The design of the second Si-wafer positioned at |z| = 640 mm, and the 2 X_0 LYSO bars mounted on the flanges are also shown. The inner radius of the second Si-wafer is 12 mm, while the outer radius is 51 mm. The dimensions of the front LYSO bars are $3 \times 3 \times 23$ mm³, while the outer radius of the overall module is 56 mm. The long LYSO modules located behind the bellow are segmented into $10 \times 10 \times 150$ mm³ blocks. The outer radius of the long LYSO modules is about 110 mm. The fast monitoring diamond detectors, as shown in (b), are positioned between the long LYSO modules on the sides of electron boosted direction, where the Bhabha electron rate is the highest. The "5 cm" in figure is used as the measurement scaling.

The latest design positions of the front surface of the at |z| = 1050 mm, while the LYSO bars are located in the region of between |z| = 800 mm and 950 mm. The *x-y* projection of the LumiCal is shown in Figure 3.14a, depicting the race-track beam pipe extending from of a 20 mm diameter beryllium pipe at the IP into dual copper beam pipes with a thickness of 3 mm. The LumiCal modules are positioned above and below the beam pipe. The dimensions of the components upstream of the flange are illustrated in Figure 3.14b, which also shows the second layer of Si-wafers and the LYSO bars with a radiation length of 2 X_0 .

The FastLumi detector is designed to detect single Bhabha electrons, which has the highest rate around the outgoing beam pipe. It is positioned on the +x side of the beam pipe near the

Draft VO 3.4 Luminosity measurement

cryomodule, accepting particles at a polar angle of approximately 10 mrad. Utilizing a diamond detector, the FastLumi can withstand the high radiation levels in this region. By detecting the rate of Bhabha events, it provides online luminosity measurements. The location of the diamond FastLumi detector is indicated by the yellow-marked region shown in Figure 3.14b.

3.4.2 Fast luminosity monitor

The FastLumi is designed to provide real-time feedback of beam collisions, which is crucial for steering the beam position. It is located in the region with the highest e^+e^- collision event rate, partly due to the beam crossing angle of 33 mrad. The FastLumi can assist in beam steering by observing the scattering of electrons on both *z*-sides. The integrated event rates along the *z*-positions can help monitor the *z*-position of the IP.

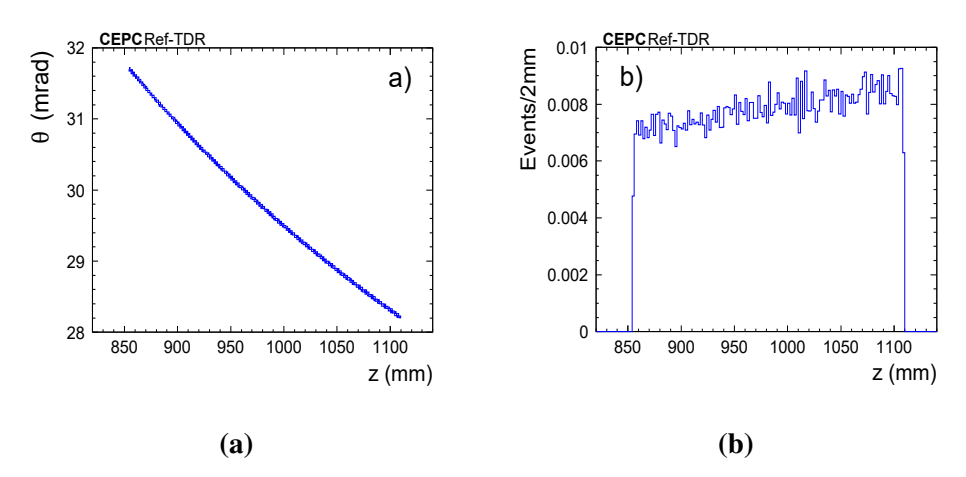


Figure 3.15: Simulation of a 50 GeV electron shower in a 3-mm-thick copper beam pipe. Results are shown for an electron incident at 10 mrad relative to the 16.5 mrad outgoing beam direction, interacting with a diamond slab ($24 \times 320 \text{ mm}^2$) positioned 13 mm from the beam center. The distribution of hits on the slab is displayed as a function of the laboratory-frame coordinates θ and z in (a), while the normalized event rate along the z-axis is presented in (b).

The FastLumi is designed with multiple microstrip detectors integrated into two slab detectors, positioned in front of the quadrupole spanning |z| = 800 to 1050 mm, a y range from -12 mm to +12 mm. It is located between the long LYSO modules, as shown in Figure 3.14a. The x position is set at +27 mm, and the detectors are slightly tilted to align closely with the beam pip. The FastLumi is positioned within a region characterized by a high radiation field. Given the high radiation levels, the most suitable detector is a segmented diamond slab detector, composed of multiple diamond-strip detectors, which is capable of detecting electron showers generated in the copper beam pipe.

Figure 3.15a illustrates a shower event of a 50 GeV electron traversing the 3-mm-thick copper beam pipe at 10 mrad. Figure 3.15b shows the Bhabha electrons from BHLUMI plotted around the beam pipe between |z| = 800 to 1050 mm. When electrons traverse the copper

Chapter 3 Machine Detector Interface and Iuminosity measurement

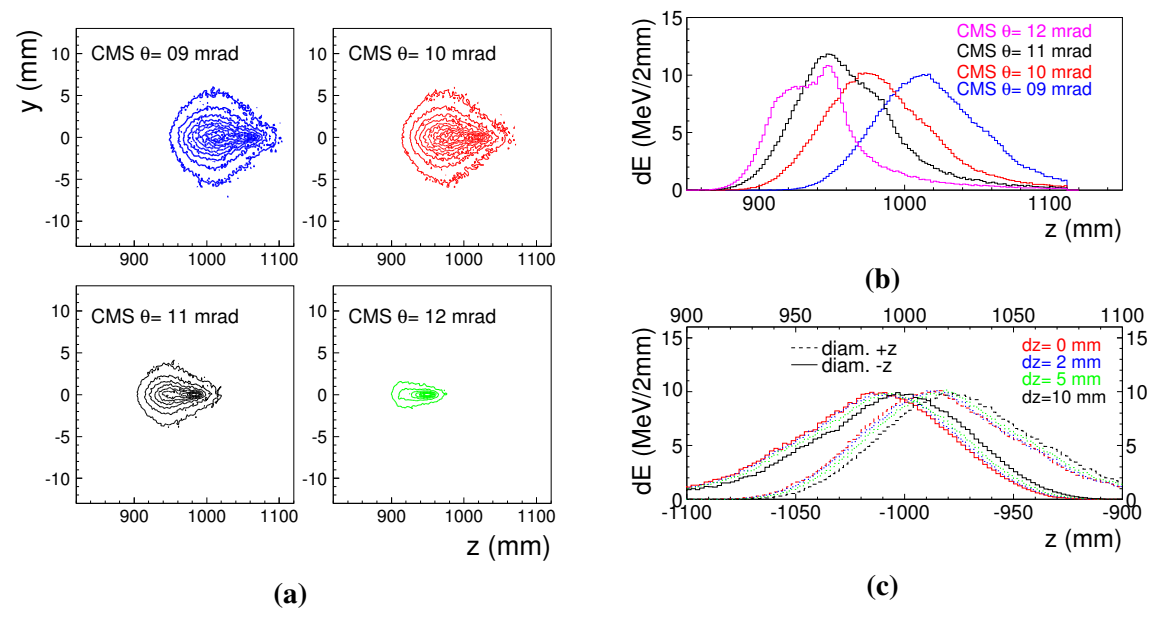


Figure 3.16: (a) Electron shower profiles of the y - z counters for CMS polar angles between 9 and 12 mrad, boosted by +16.5 mrad; (b) Energy-loss (dE/dx) deposition along z-axis. (c) Sensitivity to IP offsets: contours of the y - z shower profiles on both z sides for different values of dz.

510

511

514

515

516

517

520

521

522

523

525

526

527

528

beam pipe at small angles, most of them initiate electromagnetic showers inside the copper. The resulting secondary electrons enter the diamond detectors and deposit energy, while a smaller fraction of primary electrons pass directly through the pipe and cross the diamonds as inclined minimum-ionizing tracks. Shower simulations with 50 GeV electrons at incidence angles of 9–12 mrad are shown in Figure 3.16a, displaying broadened y–z profiles with RMS offsets of about 30 mm. In the center-of-mass system, directly incident Bhabha electrons at 15.1 mrad produce hits on at least 33 diamond strips. By applying a trigger threshold on the number of strip hits, the sum of events from showering and directly traversing electrons is used to provide fast and real time luminosity measurements. As illustrated in Figure 3.16b, the shower profiles shift systematically with the incidence angle, leading to measurable changes in both the peak position and width. For a fixed angle, different interaction point offsets result in distinct shower profiles, with the corresponding energy deposition observed in the fast luminosity monitors on both z sides, as shown in Figure 3.16c. These variations allow reconstruction of the interaction point with sensitivities of about 0.1 mm for x deviation and 10 mm for z deviation. Fast luminosity monitors placed on both z-sides further support beam steering by independently counting and comparing the Bhabha electrons at each end. Shower profiles can be analyzed on an event-byevent basis, while integrated event rates along the z-axis provide continuous monitoring of the IP position.

Diamond detectors are extensively used for beam monitoring in collider experiments [28–30]. These detectors are able to maintain low-noise operation at TID levels exceeding 10 MGy, with signal attenuation corrected through proper calibration. The newly developed synthetic

Draft vO 3.4 Luminosity measurement

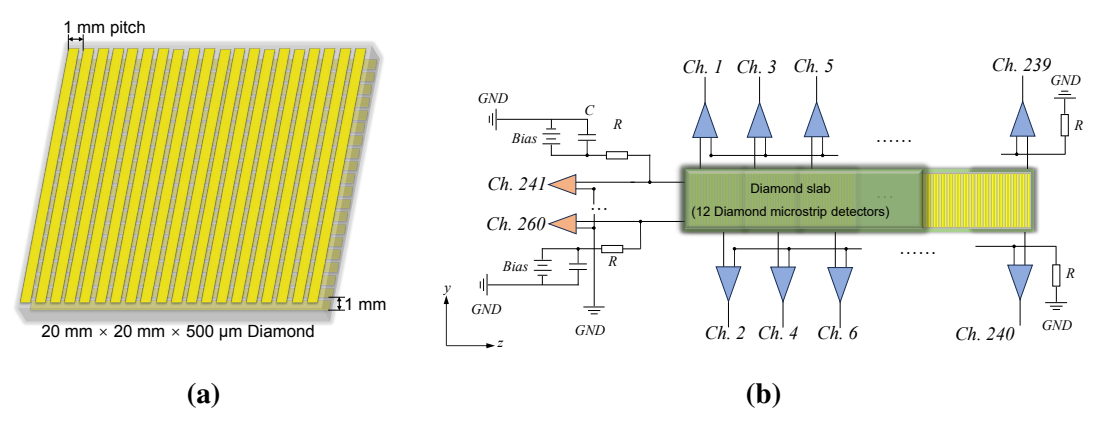


Figure 3.17: (a) Schematic of a microstrip diamond sensor with orthogonal front-side and back-side microstrips, each consisting of 0.9 mm wide strips separated by 0.1 mm gaps, forming a 1 mm pitch, as indicated by the labels; (b) Illustration of the microstrip readout for a diamond slab. The front-side microstrips (channels 1–240) are connected to preamplifiers to measure *z*-axis IP offsets, whereas the back-side microstrips (channels 241–260) are connected to high voltage to measure *y*-axis IP offsets.

diamond technology has significantly reduced defect densities, making low-cost diamonds more accessible for large-scale applications. Electronic-grade diamond crystals grown by Chemical Vapor Deposition (CVD) are used as the sensing material for the detectors. Each CVD diamond was cut into a wafer with dimensions of $20 \times 20 \text{ mm}^2$ and a thickness of $500 \text{ }\mu\text{m}$. Prior to electrode fabrication, all samples underwent standard cleaning procedure, followed by acid treatment and oxygen ion exposure to obtain an oxygen-terminated surface, which facilitates the formation of stable Ohmic contacts between the diamond and metal electrodes [31]. To achieve a spatial resolution of 1 mm for detecting Bhabha scattering electrons, microstrip electrodes were patterned on both sides of the diamond. Each strip is 19 mm long and 0.9 mm wide, with a 0.1 mm gap, giving a 1 mm pitch. The Ti/W/Au multilayer electrodes ensure low contact resistance and uniformly cover the diamond surfaces, with the front and back microstrips arranged orthogonally to enable position sensitivity in two dimensions. Each sensor surface contains 20 readout strips, as illustrated in Figure 3.17a.

Each diamond slab consists of 12 diamond sensors placed side by side along the z-axis. The front sides of these sensors together form a total of 240 microstrips with a 1 mm pitch, corresponding to readout channels 1 to 240. The backside electrodes, oriented parallel to the beam pipe, are interconnected to form 20 combined readout channels numbered 241 to 260. The diamond sensors are sandwiched between two radiation tolerant, ceramic based high frequency printed circuit boards. The metal electrodes on the diamond and the pads are bonded together and encapsulated with non-conductive epoxy to ensure mechanical stability and electrical insulation. The backside electrodes of the assembled detector are connected to a high voltage supply. The applied electric field, typically from 1 to 2 V/ μ m, guarantees full ionization charge collection efficiency. For a minimum ionizing particle traversing diamond, ionization produces on average

Chapter 3 Machine Detector Interface and luminosity measurement

36 e-h pairs/μm. When a Bhabha electron traverses the diamond at small angles, at least 32,400 charges are generated in the bulk volume beneath each 0.9 mm electrode pitch, corresponding to 5.2 fC under full collection efficiency. Micro-coaxial cables are connected to the printed circuit boards, providing both high-voltage bias and signal readout paths. The overall readout circuits are illustrated in Figure 3.17b. The signals from individual channels are preamplified, filtered, and discriminated to identify characteristic signal patterns and compute the corresponding count rates. The front-side and back-side electrodes are oriented perpendicular and parallel to the *z*-direction respectively, enabling the identification of the electron shower centers. By balancing the spectra of diamond slabs on both sides of the IP, the *x*- and *y*-positions of the electron beams and the IP position in the *z*-axis can be tuned and monitored with an angular precision of 1 μrad relative to the LumiCal.

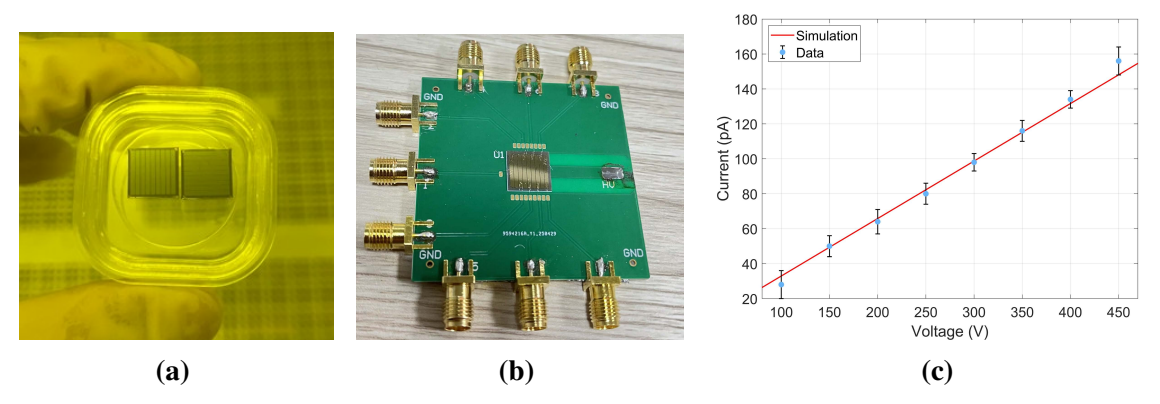


Figure 3.18: (a) Photolithography pattern in the resist after development, defining the 1 mm-pitch strip structure on the diamond prototype sensor; (b) Diamond sensor after fabrication of the metal strip electrodes, with each electrode wire-bonded to the readout; (c) I–V characteristics of the prototype sensor.

A diamond test module was fabricated from a $10\times10~\text{mm}^2$ diamond substrate grown by CVD. The substrate was cut, thinned, and polished to a thickness of approximately 300 μm , followed by surface cleaning and oxidation. Strip electrodes with 1 mm pitch were patterned on the surface (Figure 3.18a) using micro-fabrication processes, and subsequently wire-bonded to a Rogers PCB for readout as shown in Figure 3.18b. Figure 3.18c shows the measured current-voltage characteristics of the diamond test module together with results from semiconductor device simulations. The module exhibits low leakage current under an applied field of $1~\text{V}/\mu\text{m}$, the dark current remains in the range of 100--200~pA. The full diamond slab prototype and the associated beam tests are currently in progress and will be completed in the next stage.

In addition, a set of 1 cm \times 3 cm SiC detectors is introduced to measure the electrons or positrons originated from the RBB events at dedicated positions for accelerator tuning, as discussed in Ref. [32, 33]. The design of both the sensor and the entire system is on-going.